

# A Scalable Multicore Architecture With Heterogeneous Memory Structures for Dynamic Neuromorphic Asynchronous Processors (DYNAPs)

Saber Moradi<sup>1</sup>, Ning Qiao<sup>2</sup>, *Member, IEEE*, Fabio Stefanini<sup>3</sup>, and Giacomo Indiveri<sup>4</sup>, *Senior Member, IEEE*

**Abstract**—Neuromorphic computing systems comprise networks of neurons that use asynchronous events for both computation and communication. This type of representation offers several advantages in terms of bandwidth and power consumption in neuromorphic electronic systems. However, managing the traffic of asynchronous events in large scale systems is a daunting task, both in terms of circuit complexity and memory requirements. Here, we present a novel routing methodology that employs both hierarchical and mesh routing strategies and combines heterogeneous memory structures for minimizing both memory requirements and latency, while maximizing programming flexibility to support a wide range of event-based neural network architectures, through parameter configuration. We validated the proposed scheme in a prototype multicore neuromorphic processor chip that employs hybrid analog/digital circuits for emulating synapse and neuron dynamics together with asynchronous digital circuits for managing the address-event traffic. We present a theoretical analysis of the proposed connectivity scheme, describe the methods and circuits used to implement such scheme, and characterize the prototype chip. Finally, we demonstrate the use of the neuromorphic processor with a convolutional neural network for the real-time classification of visual symbols being flashed to a dynamic vision sensor (DVS) at high speed.

**Index Terms**—Asynchronous, circuits and systems, neuromorphic computing, routing architectures.

## I. INTRODUCTION

IN AN effort to develop a new generation of brain-inspired non von Neumann computing systems, several neuromorphic computing platforms have been proposed in recent years, that implement spike-based re-configurable neural networks [1]–[8]. Despite being developed with different goals

in mind and following different design strategies, most of these architectures share the same data representation and signal communication protocol: the Address-Event Representation (AER) [9], [10]. In this representation computational units (e.g., neurons) are assigned an address that is encoded as a digital word and transmitted as soon they produce an event (e.g., as soon as the neuron spikes) using asynchronous digital circuits. Information is therefore encoded in the timing of these address-events. In event-based neural networks the neurons inter-spike interval (the interval between successive address events produced by the same neuron) represent the analog data, and neural computation is achieved by connecting multiple neurons among each other with different types of connectivity schemes. Spike produced by source neurons are transmitted to one or more destination synapse circuits that integrate them with different gain factors and convey them to the post-synaptic neuron. Unlike classical digital logic circuits, these networks are typically characterized by very large fan-in and fan-out numbers. For example, in cortical networks neurons project on average to about 10000 destinations. The type of processing and functionality of these spiking neural networks is determined by their specific structure and parameters, such as the properties of the neurons or the weights of the synapses [11]. It is therefore important to design neuromorphic computing platforms that can be configured to support the construction of different network topologies, with different neuron and synapse properties. This requires the development of configurable neuron and synapse circuits and of programmable AER routing and communication schemes. The latter elements are particularly important, because the scalability of neuromorphic systems is mainly restricted by communication requirements. Indeed, some of the main bottlenecks in the construction of large-scale re-configurable neuromorphic computing platforms are the bandwidth, latency, and memory requirements for routing address-events among neurons. Most large-scale neuromorphic computing approaches followed up to now have either restricted the space of possible network connectivity schemes to optimize bandwidth usage while minimizing power and latency [3], [12], or have designed systems that use large amounts of memory, silicon real-estate, and/or power, to maximize flexibility and programmability [4], [5]. In particular, most approaches proposed either make use of 2D mesh routing schemes, with maximum flexibility, but at the cost of large resource usage, or tree routing schemes which minimize latency

Manuscript received April 1, 2017; revised August 9, 2017; accepted September 20, 2017. Date of publication November 3, 2017; date of current version January 26, 2018. This work was supported by the EU ERC Grant “neuroP” (257219) and by the EU ICT Grant “NeuRAM<sup>3</sup>” (687299). This paper was recommended by Associate Editor Dr. Philipp Häfliger. (*Corresponding author: Saber Moradi.*)

S. Moradi is with the Computer Systems Laboratory, School of Engineering and Applied Science, Yale University, New Haven CT 06520 USA (e-mail: saber.moradi@yale.edu).

F. Stefanini is with the Center of Theoretical Neuroscience, Columbia University, New York, NY 10027 USA (e-mail: fs2545@cumc.columbia.edu).

N. Qiao and G. Indiveri are with the Institute of Neuroinformatics, University of Zurich, 8057 Zurich, Switzerland, and also with ETH Zurich, 8092 Zurich, Switzerland (e-mail: qiaoning@ini.uzh.ch; giacom@ini.uzh.ch).

Color versions of one or more of the figures in this paper are available online at <http://ieeexplore.ieee.org>.

Digital Object Identifier 10.1109/TBCAS.2017.2759700

and power, but are more restrictive in the types of networks that can be supported (see [13] for a comprehensive overview comparing most of the approaches that have been proposed in the literature). In [13] the authors proposed a *hierarchical* address event routing scheme (HiAER) that overcomes some of the limitations of previous flat tree-based approaches. However, as with many of the previous approaches [5], the HiAER architecture stores the routing tables in external memory banks implemented using Dynamic Random Access Memory (DRAM). Within this context, these approaches do not represent a radical departure from the classical von Neumann architecture, as they are affected by the von Neumann bottleneck problem [14], [15].

In this paper we propose a radically new routing scheme that integrates within the arrays of neurons and synapses both asynchronous routing circuits and heterogeneous memory structures used to store the data as distributed programmable routing tables. The routing scheme has been obtained by analyzing all previous approaches, and carrying out a systematic study for minimizing memory resources and maximizing network programmability and flexibility. The approach we propose combines the advantages of all previous approaches proposed up to now by combining 2D-mesh with hierarchical routing, implementing a 2-stage routing scheme for minimizing memory usage, which employs a combination of point-to-point source-address routing and multi-cast destination-address routing, and by using heterogeneous memory structures distributed within and across the neuron and synapse arrays which are optimally suited to exploit emerging memory technologies such as Resistive Random Access Memory (RRAM) [16].

In the Section II we present the theory that was developed to minimize memory requirements in multi-neuron architectures. In Section III we describe the mixed mode hierarchical-mesh routing scheme proposed, and the Quasi Delay Insensitive (QDI) circuits designed to implement them; in Section IV we present a multi-core neuromorphic chip that was designed and fabricated to validate this routing scheme. The chip comprises 1k VLSI neurons distributed among four neural cores and programmable routers for managing the AER traffic. The routing fabric implemented in this chip uses new designs of quasi-delay insensitive asynchronous circuits, synthesized following the Communicating Hardware Process (CHP) formalism, while the neural and synaptic dynamics are designed using ultra-low power subthreshold neuromorphic circuits [17]. Finally, in Section V we demonstrate an application of this architecture by configuring the neuromorphic processor to implement a Convolutional Neural Network (CNN) designed to process fast sequences of visual patterns, represented by Address-Events (AEs) that are generated by a Dynamic Vision Sensor (DVS) for low latency classification. We conclude the paper by comparing the features of the circuits and approach proposed to the current state-of-the-art and discuss the benefits of the proposed architecture.

## II. MEMORY OPTIMIZED ROUTING

Consider a generic spiking neural network with  $N$  neurons in which each neuron has a large fan-out of  $F$ . This is the case

for many neural network models including biologically plausible models of cortical networks, recurrent neural networks, convolutional networks and deep networks. In standard routing schemes e.g., source or destination-based methods, each neuron would be assigned a unique address encoded with  $\log_2(N)$  bits. Therefore, to support  $F$  fan-out destinations per neuron, a storage of  $F \log_2(N)$  bits/neuron would be required. In total, the size of the connection memory the whole network would then be  $NF \log_2(N)$ . While this scheme can support any type of connectivity, it is very wasteful in case of networks that have a specific structure, i.e., for most of the real and artificial neural networks [18], [19].

Inspired by the connectivity patterns in biological neural networks [20], [21] we developed a novel routing scheme that exploits their clustered connectivity structure to reduce memory requirements in large-scale neural networks. This novel method uses a mixed tag-based shared-addressing scheme, instead of plain source or destination addressing schemes. The main idea is to introduce different clusters with independent address spaces, so that it is possible to re-use the same tag ids for connecting neurons among each other, without loss of generality. Specifically, in the proposed routing method neurons are grouped in separate  $N/C$  clusters of size  $C$ , and the connectivity with destination nodes (i.e., the fan-out operation) is divided into two distinct stages [22]. In the first stage, the neurons use source-address routing for targeting a subset ( $F/M$ , with  $F > M$ ) of the intermediate nodes. The number of intermediate nodes is  $N/C$  (with  $F/M \leq N/C$ ). In the second stage the intermediate nodes broadcast the incoming events for targeting a number  $M \leq C$  of destination neurons within each local domain (or cluster)  $C$  (see Fig. 1). Each neuron in the end-point cluster uses a set of *tags* (one of  $K$  tags for the cluster) to determine whether to accept or ignore the AER packet received. In addition to distributing the memory resources among multiple nodes (neurons) within the computing fabric, therefore eliminating the von Neumann bottleneck [14], [15], this two-stage routing scheme allows us to minimize the total digital memory for configuring the network connectivity,<sup>1</sup> still allowing for large  $M$ -way fan-out: the total memory  $MEM$  required per neuron can be separated into *Source memory*  $MEM_S$  and *Target memory*  $MEM_T$ . At the sender side each source neuron stores  $F/M$  entries. Each of these entries has two fields: the first field requires  $\log_2(K)$  bits for representing a source tag and the second requires  $\log_2(N/C)$  bits to represent the address of the target intermediate nodes (see also Fig. 1). Therefore the total *Source memory* required is  $MEM_S = (F/M)(\log_2(K) + \log_2(N/C))$  bits/neuron. At the destination side, assuming that the tags are uniformly distributed, each neuron needs to store  $M$  tags. This leads to using  $KM$  tag entries per cluster and  $KM/C$  tags per neuron, with each tag requiring  $\log_2(K)$  bits. As a consequence, a total *Target memory* of  $MEM_T = (KM/C)(\log_2(K))$  bits/neuron is required. Taking into account these values,

<sup>1</sup>provided that  $M \leq F$  and  $M \leq C$  – see Appendix A for an in-depth analysis of the feasibility of these constraints.

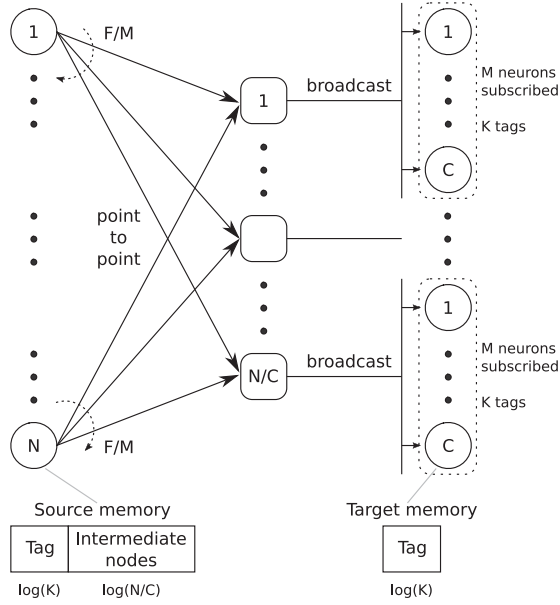


Fig. 1. Two-stage tag-based routing scheme. The connectivity of a network of  $N$  neurons with fan-out  $F$  is implemented by a scheme that uses  $N$  neurons with a reduced fan-out of  $F/M$  that transmit their tag data to  $N/C$  intermediate nodes, with point-to-point routing. Each intermediate node broadcasts its tag data to all neurons of its target cluster. Each cluster has  $C$  neurons, with a subset of  $M$  neurons subscribed to the incoming tag. The total unique number of tags used in each cluster is  $K$ . Note that the nodes on the right side represent the same neurons of the left side, but grouped into  $N/C$  clusters.

we get:

$$MEM = MEM_S + MEM_T \quad (1)$$

$$MEM = \frac{F}{M} \log_2 \left( \frac{KN}{C} \right) + \frac{KM}{C} \log_2(K). \quad (2)$$

As evident from (2), larger clusters and fewer tags lead to reduced memory requirements. Reducing the number of tags reduces the routing flexibility. However this can be counter balanced by increasing the number of clusters. By considering the ratio  $\alpha = K/C$  it is possible to minimize for memory usage while maximizing for routing flexibility: if we substitute  $K = \alpha C$  in (2), we get:

$$MEM = \frac{F}{M} \log_2(\alpha N) + \alpha M \log_2(\alpha C). \quad (3)$$

The parameter  $M$  determines the trade-off between point-to-point copying in the first stage versus broadcasting in the second stage of the routing scheme. The total memory requirement can therefore be minimized by differentiating (3) with respect to  $M$ , and determining the optimal  $M^*$ :

$$0 = \alpha \log_2(\alpha C) - \frac{F}{M^2} \log_2(\alpha N) \quad (4)$$

$$M^* = \sqrt{\frac{F \log_2(\alpha N)}{\alpha \log_2(\alpha C)}}. \quad (5)$$

With this choice of  $M$ , the total number of bits per neuron required are  $MEM = 2\sqrt{\alpha F \log_2(\alpha C) \log_2(\alpha N)}$ . If for example we set, as a design choice,  $\alpha = 1$ , then we obtain  $M^* = \sqrt{F \log_2(N) / \log_2(C)}$ . This leads to a total memory/neuron

requirement of:

$$MEM = 2\sqrt{F \log_2(C) \log_2(N)}. \quad (6)$$

We therefore developed a scheme in which the memory requirements scale with  $N$  in a way that is drastically lower than the scaling of standard routing schemes, that require  $F \log_2(N)$  bits/neuron (e.g., compare 160 k bits/neuron of memory for a network of approximately 1 million ( $2^{20}$ ) neurons, with fan-out of almost 10000 ( $2^{13}$ ) required with the conventional routing approach, versus less than 1.2 k bits/neuron required for our memory-optimized scheme, for a network of same size, with same fan-out, and with cluster size of 256 neurons). Unlike basic source or destination based routing methods, the scheme we developed is a mixed one that makes use of tag addresses which are shared among source and destination neurons. This results in a much smaller address space required to encode the connections among neurons and fewer memory entries to support large fan-out in biologically plausible clustered neural networks.

### III. MIXED-MODE HIERARCHICAL-MESH ROUTING ARCHITECTURE

In this section we propose a multi-core routing architecture that deploys the memory optimization scheme of Section II: each cluster of Fig. 1 is mapped onto a “core”, the intermediate nodes are implemented by asynchronous routers, and the tags are stored into asynchronous Content Addressable Memory (CAM) blocks. The CAM block of each neuron contains multiple tags representing the address of sources that this neuron is subscribed to.

To optimize the event routing within the network, we adopted a mixed-mode approach that combines the advantages of mesh routing schemes (low bandwidth requirements, but high latency), with those of hierarchical routing ones (low latency, but high bandwidth requirements) [3]. Specifically, this architecture adopts a hierarchical routing scheme with three distinct levels of routers: at the lowest level an R1 is responsible for the local traffic, it either sends back the events to its source core or to the next level of hierarchy. The events sent from the R1 router to its local core are broadcast to all nodes within the core; following the prescription of the scheme described in Section II. Incoming events are presented to the CAM blocks of all neurons and if there is match in the CAM they will be accepted by the nodes as valid inputs. The events targeting different cores are sent to the second level router (R2) which has bidirectional channels to communicate with local cores and the next level router. Depending on the complexity of the network, this tree-based routing structure can have multiple R2 levels (e.g., see Fig. 2 for an example with three R2 levels). For transmitting data packets across even longer distances, the highest level router (R3) is employed, which uses a relative 2D-mesh (also known as xy algorithm) routing strategy. A combination of R1, R2, and R3 routers represent the intermediate nodes of Fig. 1, the cores represent the clusters, the *Source memory* is stored in Static Random Access Memory (SRAM) cells in the R1 routers, and the *Target memory* in the synapse CAM cells. For the prototype described in this paper, we have chosen three level of routing.



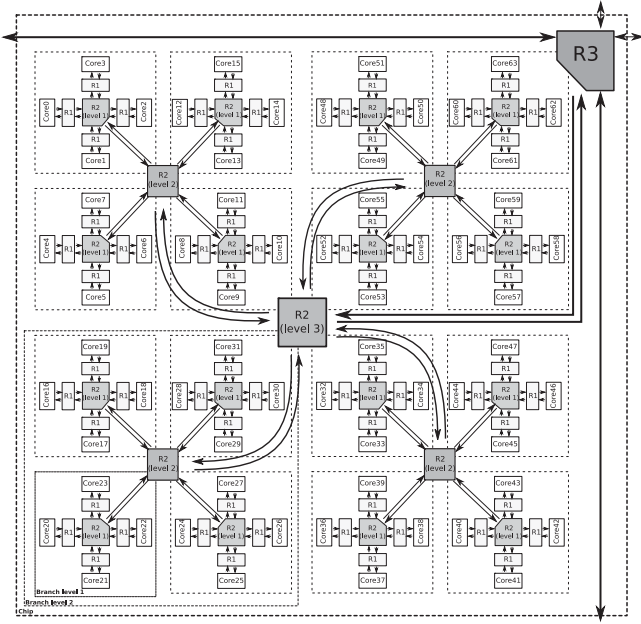


Fig. 2. Mixed-mode hierarchical-mesh routing network example. At the lowest level, single cores transmit and receive events via broadcast operations through a “R1” router. Groups of four cores are linked together by a level-1 “R2” router. To reach cores belonging to different groups (but for example on the same tile), it is possible to use “level-2” or higher level R2 routers, following a tree-based routing strategy. To reach even further destinations (e.g. on different tiles), it is possible to use an “R3” router, which transmits signals along four cardinal directions using a 2D-mesh routing strategy.

#### A. Quasi Delay-Insensitive Asynchronous Circuit Design Methodology

The asynchronous circuits that implement the R1, R2, and R3 routers, and the overall routing architecture, were synthesized using the QDI approach [23], by following the Communicating Hardware Processes (CHP) [24] and Handshaking Expansion (HSE) formalism [25] (see also Appendix C for the most common CHP commands). The QDI circuit design methodology only makes timing assumptions on the propagation delay of signals that fan-out to multiple gates, but makes no timing assumption on gate delays. The CHP language provides a set of formal constructs for synthesizing a large class of programs [26]. Similarly, a Handshaking Expansion program is an intermediate representation of CHP constructs in order to close the gap between the high-level representation i.e. CHP and the low-level circuit description of the system. At this stage of design flow, handshaking protocol and additional restrictions on variable type and assignment statements are introduced into CHP program to allow the designer to reach a level of description that is closer to the desired circuit netlist of the system. Finally, HSE programs are transformed into a set of “production rules” which are abstract descriptions of digital Complementary Metal-Oxide-Semiconductor (CMOS) Very Large Scale Integration (VLSI) circuits [25]. As example of asynchronous circuit synthesis, we provide a complete set of CHP, HSE, and production rule commands for building a QDI “Controlled-pass” process. This specific process is commonly used for implementing the routers, and comprises both control flow as well as data-path

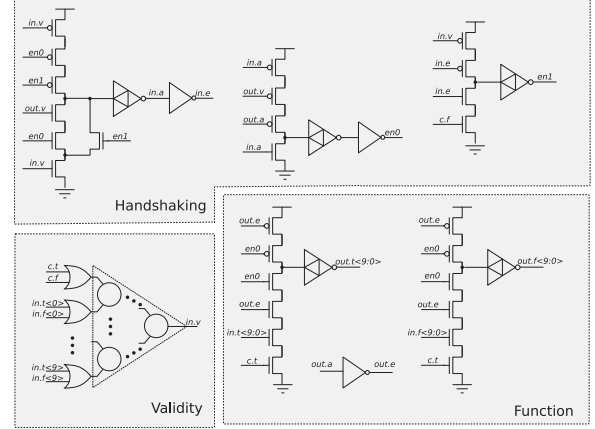


Fig. 3. “Controlled-pass” QDI circuit diagram. The CMOS circuit is derived based on the production rules of Listing 3. The circles in the circuit represent C-elements.

circuits. The “Controlled-pass” process has two input channels *in*, *sig* and one output channel *out*. The *in* channel holds the input data and the *sig* channel represents a one bit control signal which decides whether to copy the data from *in* channel to *out* channel or not. In other words this process copies the input to the output if *sig* is *True* and skips otherwise. The *sig* channel is encoded with dual-rail representation: it uses two physical signals *sig.t* and *sig.f* to represent a single bit of information. As the *sig.t* and *sig.f* signals cannot be both *True* at the same time (dual-rail encoding), the decision (pass or not pass) can be made using a *deterministic selection* without the need for arbitration. In the CHP program example of Listing 1, the process first waits for a new token to arrive on the input channel ( $[v(in)]$  becomes true) and checks the value of *sig* signal. In the case of *sig.t* : *true* the process sets the output channel ( $out.d \uparrow$ ) and waits for the input and the sign signals to become neutral ( $[n(in) \wedge n(sig)]$ ). Only then the process releases the output signals ( $out.d \downarrow$ ). If on the other hand *sig.f* is true, then the process skips further computations. Fig. 3 shows the Controlled-pass process circuit diagrams derived from Listing 3.

```

chp {
  *[[v(in)];
  [sig.t → out.d↑; [n(in) ∧ n(sig)]; out.d↓;
  []
  sig.f → skip; [n(in) ∧ n(sig)];
  ]
}

```

Listing 1: Controlled pass: CHP.

```

hse {
  *[[ sig.t → out.b[i].d[j] := in.b[i].d[j]; in.a
  +; en0-;
  ([out.a]; out.b[i].d[j]-; [~out.a]), ([n(in)];
  in.a-); en0+
  []
  sig.f → en1+; in.a+; [n(in)]; en1-; in.a-;
  ]]
}

```

Listing 2: Controlled pass: HSE.

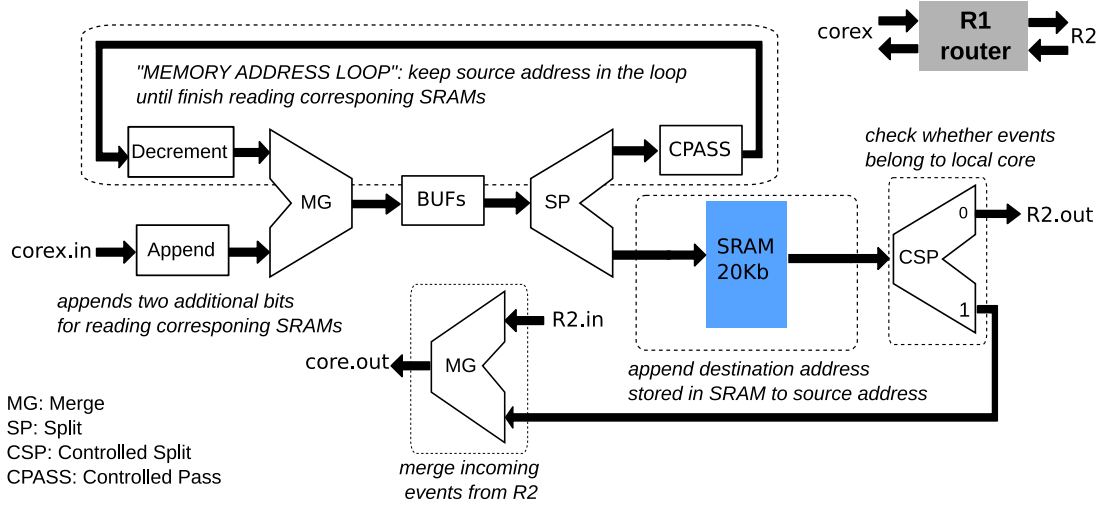


Fig. 4. Block diagram of the R1 router. There is one R1 router/core. Each R1 router has a bidirectional link between itself and its local core, and a bidirectional link between itself and its R2 router.

```

prs {
  in.v & (en1 | out.v) → in.a+
  ~en1 & ~en0 & ~in.v & ~sig.f & ~sig.t → in.a-

  ~in.a & ~out.a & ~out.v → en0+
  in.a → en0-

  in.e & sig.f → _en1-
  ~in.e & ~in.v → _en1+

  _en → en1-
  ~_en1 → en1+

  (: i:0..N:
    (: j:0..1:
      en0 & in.b[i].d[j] & sig.t → out.b[i].d[j]+
      ~en0 & out.e → out.b[i].d[j]-
    )
  )
}

```

Listing 3: Controlled pass: PRs.

### B. Asynchronous Routing Fabric

In the following we describe the block diagrams of the QDI routing architecture implemented following CHP design methodology. As an example design choice, we assign 256 neurons/core (i.e.,  $C$  of Fig. 1 is set to 256), and four cores/tile (i.e.,  $M$  is set to 4); we assume that each neuron can copy its output to four different destination cores; and, for sake of simplicity, we assume that one tile corresponds to a single VLSI chip, which requires only one level of R2 arbiters in the hierarchy.

1) *The R1 Router:* Each core in the chip is paired to a R1 router, and each R1 router has an embedded SRAM of size proportional to the number of source nodes in the core. The block-diagram of the R1 router is shown in Fig. 4. Address-events generated by neurons in the corresponding core “x” are sent to R1 (see *corex.in* signal). The data packet representing the address-event is extended, by appending two additional bits that encode the fan-out for the first-level point-to-point copy (equivalent to  $F/M$  in Section II). The extended packet then enters the

“memory address loop” of Fig. 4, which comprises a QDI merge, a buffer, and a split process, as well as a controlled-pass and a decrement process. The merge process is non-deterministic: it does arbitration on two input requests and allows the winner to send its message through to the output. Initially the input data packet is copied, via the merge process to a buffer and then split into two branches: the bottom output of the split process is used to address an asynchronous SRAM block, and read the content of the addressed memory; while the upper output of the split process is fed to the controlled-pass process of the feed-back loop. The controlled-pass checks the header bits (the two bits appended in previous stage) and passes the packet through if the header value is non-zero, otherwise it skips. When passed, the value of header bit is decremented and then merged back to the forward path, in order to read the next address of the SRAM. This “memory loop address” process continues until all memory information for the corresponding event is read.

The content of each SRAM cell is a 20-bit word, which includes a 10-bit tag address, a 6-bit header information, and a 4-bit destination core id. The 6-bit header uses 2-bits to encode the  $\Delta X$  number of hops, 2-bits for the  $\Delta Y$  hops, one sign bit for the  $X$  direction (east or west) and one for the  $Y$  directions (north or south). A controlled split process after the SRAM checks the core and chip destination address bits, and decides whether to broadcast the data back to the same core, to send it point-to-point to a different core on the same chip, or to send it via mesh-routing to a core on a different chip through the R2 and R3 routers. The controlled split is a one-input to two-output process where control bits decide which output receives the input data, unlike a normal split process where incoming data are sent to both outputs.

2) *The R2 Router:* Each R2 router has four bidirectional links to R1 routers of the same level of the cores in the chip and one bidirectional link to the higher level router. This router manages both the inter-tile communication and the communication with longer distance targets (see Fig. 5). Based on a hierarchical 2D tree architecture, this router is at the heart of

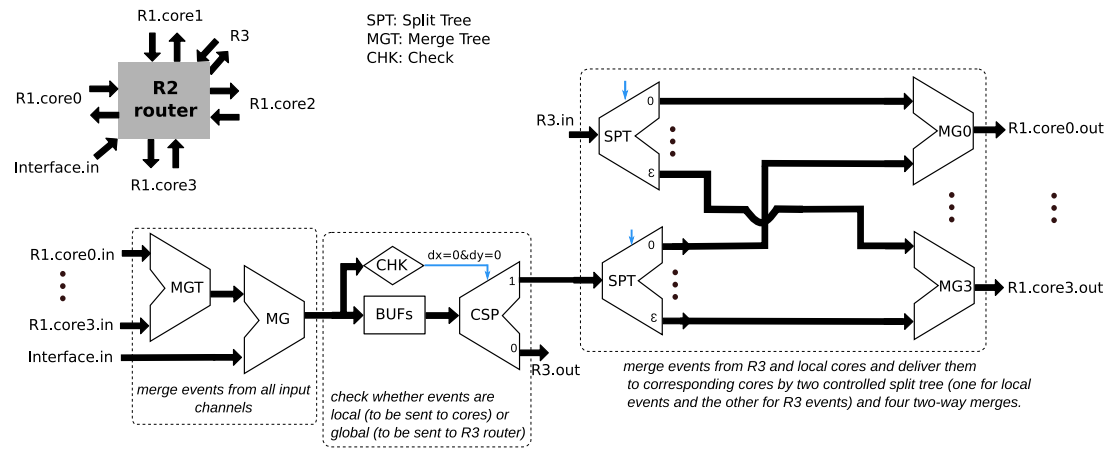


Fig. 5. Block diagram of the R2 router. This router has bidirectional links with four R1 routers in the same chip, and one bidirectional link with higher level router for managing inter-chip traffic.

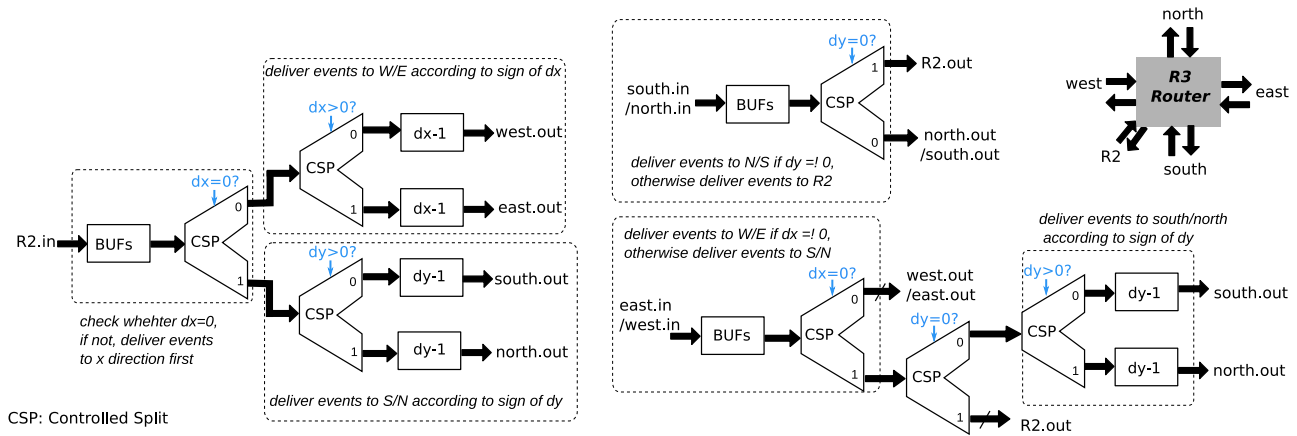


Fig. 6. Block diagram of the R3 router. There is one R3 router per chip/tile to manage global traffic in a 2D-mesh of chips/tiles.

the proposed routing scheme. At each level of the tree hierarchy there is one bidirectional link between R2 and each core in the same level (total 4) and one bidirectional link between R2 and the higher-level router. With the design choices we made for these block diagrams, the next level in the hierarchy is directly represented by an R3 router. Data from all the incoming R1 channels ( $R1.core0.in - R1.core3.in$ ) is first merged into a single stream by a merge tree. Then by checking the 6-bit chip destination address entries of the packet, it determines whether to route events to the higher level inter-chip router via  $R3.out$  port, or to redirect events to one of the local R1 routers. In the latter case, a controlled split tree decides which local core to target. Similarly, on the downstream pathway, the R2 router receives events from the R3 router (see  $R3.in$ ) and a controlled split tree decides which destination core to target, using the destination core id specified in the packet's header.

3) *The R3 Router*: This block routes events among multiple tiles with relative distance addressing along a 2D-mesh. The block diagram of R3 router is illustrated in Fig. 6. On one side, this router communicates with its lower-level R2 router in same tile, and on other side it communicates with other four R3 routers of other chips/tiles in a global 2D-mesh network following an

“XY routing” method. This method first routes events in X direction until  $\Delta X$  is decremented to zero, and then in the Y direction.

On the upstream pathway, the router buffers the signals  $R2.in$ , and performs a control split operation: it first checks  $\Delta X \neq 0$ , and if yes sends the data to the west port (if  $signX > 0$ ) or to the east port (if  $signX < 0$ ). If the value of  $\Delta X = 0$  the events are sent to the north or south ports, depending on the value of  $\Delta Y$ . As events are passed through, the corresponding  $\Delta X$  and/or  $\Delta Y$  values are decremented by one. There are two bits  $signX$  and  $signY$  in the packet that specify the sign of  $\Delta X$  and  $\Delta Y$  changes. On the downstream pathway, events can arrive from the south/north ports, or from the east/west ones. In the first case, south/north input events trigger a check of the value of  $\Delta Y$ , done by a controlled split process. If this value is zero, the events are sent to the local R2 router (see  $R2.out$  in Fig. 6). Otherwise they are sent to the north/south link. In the case of incoming events from south/north ports, the  $\Delta X$  value is not checked as it will always equal to zero. In the case of an event reaching the east/west port, this triggers a control split process to check the value of  $\Delta X$ . If this is not zero, it is passed onto the west/east port and processed as described above, otherwise

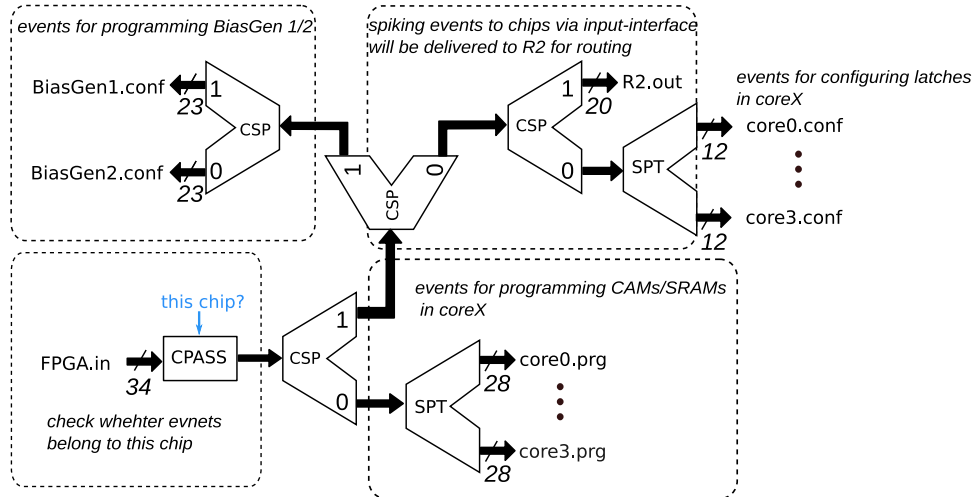


Fig. 7. Input Interface block for programming on-chip SRAM and CAM memories, and for configuring additional network parameters.

a check is made on the  $\Delta Y$  value, via a second split control process. Depending on the value of  $\Delta Y$  the data is passed onto the south/north port, and  $\Delta Y$  is decremented.

4) *Input Interface*: This additional QDI block is used for sending stimuli to the neurons in the cores from external sources of address-events, to program the distributed SRAM and CAM memory cells, to set additional network configuration parameters, and to configure different circuit biases (see Fig. 7). Once address-events reach this block (e.g., from a Field Programmable Gate Array (FPGA) device, via the *FPGA.in* signals), a first check is made to see if the data packet contains the correct chip/tile address. If so, the data packet is first checked via a control split process to see if the data represent programming or configuration commands, or normal address-events. In the latter case, the data is sent directly to the destination core. Otherwise the data packet goes through a second control split process to check if it represent control words for programming bias generators, or data for programming the memory cells. Additional control split processes keep on making checks on the data, until it is delivered to its final destination, which could be a register for programming on chip bias generators (for example), or an SRAM or CAM cell memory content.

#### IV. A MULTI-CORE NEUROMORPHIC PROCESSOR PROTOTYPE

We validated the architecture proposed by designing, fabricating, and testing a prototype multi-core neuromorphic processor, made adopting the design choices used in Section III-B: the chip comprises four cores; each core comprises 256 neurons, and each neuron has a fan-out of 4 k. It has hierarchical asynchronous routers (R1, R2, and R3 level), and embedded asynchronous SRAM and CAM memory cells, distributed across the cores and the routers. Following the memory-optimizing scheme of Section II, the communication circuits combine point-to-point source-address routing with multi-cast destination-address routing, and use a mixed-mode hierarchical-mesh connectivity fabric.

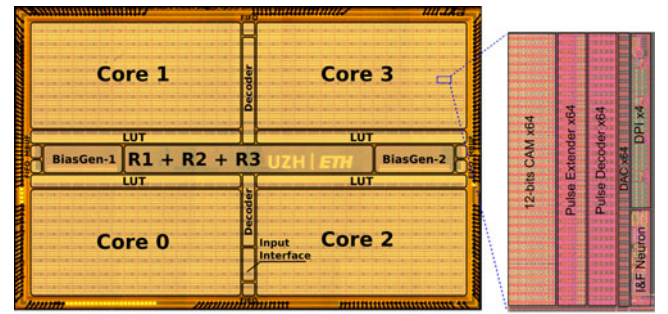


Fig. 8. Die photo of the multi-core neuromorphic processor. The chip comprises four cores, each with 256 neurons. Neurons belonging to different cores, and to different chips can interact among each other via the R1, R2, and R3 routers. Neuron and synapse dynamics can be programmed via the on-chip bias generators.

The chip was fabricated using a standard 0.18  $\mu\text{m}$  1P6M CMOS technology, and occupies an area of 43.79  $\text{mm}^2$  (see Fig. 8 for the chip micro-graph). The memory optimization theory and the hierarchical routing fabric can be used with either pure digital logic approaches [4], or mixed mode analog/digital ones [17]. Here we demonstrate a neuromorphic processor designed following a mixed signal approach: we implemented the neuron and synapse functions and state-holding properties using parallel analog circuits, rather than time-multiplexed digital ones. The analog circuits are operated in the sub-threshold domain to minimize the dynamic power consumption and to implement biophysically realistic neural and synaptic behaviors, with biologically plausible temporal dynamics [17].

The core area of the chip layout (excluding pad frame) measures 38.5  $\text{mm}^2$ , of which approximately 30% is used for the memory circuits, and 20% for the neuron and synapse circuits (see Table I for a detailed breakdown of the area usage). Neurons are implemented using Adaptive-Exponential Integrate and Fire (AdExp-I&F) neuron circuits of the type described and fully characterized in [2]. The circuit comprises a block implementing N-Methyl-D-Aspartate (NMDA) like voltage-gating, a leak block implementing neuron's leak conductance, a negative



TABLE I  
DETAILED AREA BREAKDOWN OF THE CHIP'S CIRCUIT BLOCKS

Block name	Silicon area%
On-chip memory	31.7%
Pulse extenders and decoders	25.2%
Neurons and synapses	22.8%
Routers	9.7%
Bias generators	6.4%
Other	4.3%

The core area of the chip is  $38.5 \text{ mm}^2$ .

feedback spike-frequency adaptation block, a positive feedback block which models the effect of Sodium activation and inactivation channels for spike generation, and a negative feedback block that reproduces the effect of Potassium channels to reset the neuron's activation and implement a refractory period. The negative feedback mechanism of the adaptation block and the tunable reset potential of the Potassium block introduce two extra variables in the dynamic equation of the neuron that endow it with a wide variety of dynamical behaviors [27], [28].

Synapses and biophysically realistic synapse dynamic are implemented using sub-threshold Differential Pair Integrator (DPI) log-domain filters, of the type proposed in [29], and described in [17]. These circuit can produce Excitatory Post-Synaptic Currents (EPSCs) and Inhibitory Post-Synaptic Currents (IPSCs) with time constants that can range from few  $\mu\text{s}$  to hundreds of ms, using relatively small capacitors (of the value of about 1 pF), thus keeping the circuit footprint to a minimum size. The analog circuit parameters governing the behavior and dynamics of the neurons and synapses are set by programmable on-chip temperature compensated bias-generators [30]. There are two independent bias-generator blocks, to provide independent sets of biases for core pairs, to allow the modeling of different neural population types. The use of mixed-mode analog/digital circuits, embedded in the asynchronous routing fabric proposed allowed us to distribute the memory elements across and within the computing modules, creating an in-memory computing architecture that makes use of distributed and heterogeneous memory elements (such as capacitors, CAM, and SRAM cells) and that is truly non-von Neumann. Alternative neuromorphic processors that use pure digital design styles typically time-multiplex the computing resources and are still faced with the problem of having to transfer state memory back and forth from areas devoted to computing to areas devoted to memory storage [4], [5].

#### A. The Core Memory/Computing Module

The block diagram of the circuits comprising the synapse memory and synapse dynamic circuits together with the neuron circuits is shown in Fig. 9. Each of these nodes implements at the same time the memory and computing operations of the architecture: there are 64 10-bit CAM words, 64 2-bit SRAM cells, four synaptic dynamics circuits, and one leaky integrate and fire neuron circuit per node. The asynchronous CAM memory is used to store the tag of the source address that the neuron is connected to, while the 2-bit SRAM memories are used to

program the type of synaptic dynamics circuit to use. Depending on the content of the SRAM a synapse can be programmed to exhibit one of 4 possible behaviors: fast excitatory, slow excitatory, subtractive inhibitory, or shunting inhibitory. Each synapse behavior is modeled by a dedicated DPI circuit, each with globally shared biases that set time constants and weight values. When a synapse accepts an address-event that has been broadcast to the core (i.e., when there is a match between the address transmitted and the one stored in the synapse CAM cell), the event triggers a local pulse-generator circuit, which in turn drives a pulse-extender circuit to produce a square wave of tunable width, ranging from fractions of  $\mu\text{s}$  to tens of ms. These square waves are then fed into the addressed DPI circuit, which integrates them over time, and produces an EPSC or IPSC with corresponding weight and temporal dynamics.

Eventually, once all synaptic currents integrated by the neuron make it cross its spiking threshold, the neuron will produce an output digital event and send it to its handshaking block (HS). This block will communicate with neuron address encoder which will transmit the address-event to the core associated R1 router.

#### B. Asynchronous Content-Addressable Memory Circuits

Fig. 10 shows a simplified diagram of the  $16 \times 16$  asynchronous CAM cells, as they are arranged in each core. Each CAM cell comprises 64 10 bit word CAM circuits, as described on the left side of Fig. 10, which contain the addresses of 64 source neurons connected to the corresponding destination neuron's synapses. The CAM cells make use of NOR-type 9T circuits and of a pre-charge-high Match-Line scheme [31]. In the pre-charge phase, no data is presented on the search bit lines (neutral state of data) and the signal *PreB* is asserted to *low*, in order to pre-charge all the Match-Lines in the core to *high*. In the search phase, *PreB* is asserted to *high* and all CAMs compare their contents with the data presented on the search lines simultaneously. A *miss* between any input data bit and the content of the corresponding CAM bit circuit discharges the corresponding match line. Thus, only CAM words with a *match* on all bits keep the corresponding Match-Line *high*. A Low-Threshold (LTH) inverter together with a weak pull-up P-MOS transistor is used to compensate the leak from the *NOR* transistors during the search phase in order to guarantee that only a real *miss* will pull the Match-Line low. After all CAM comparisons are complete, a pulse signal *Check* is transmitted across the whole core and multiplied with the Match-Lines (i.e., via a logical *AND* operation) to generate pulses for all CAM words that are in a *match* state. The matched pulses are then transmitted to the pulse generation circuit of Fig. 9, and used to produce the synaptic currents.

The search operation of the asynchronous CAM array follows a standard four-phase handshaking protocol, to communicate with the QDI routing blocks. However, to minimize its area, the interface to the CAM array make timing assumptions and does not implement a QDI design style. The full description of the asynchronous CAM circuit behavior, and of the timing assumptions made are detailed in Appendix D.



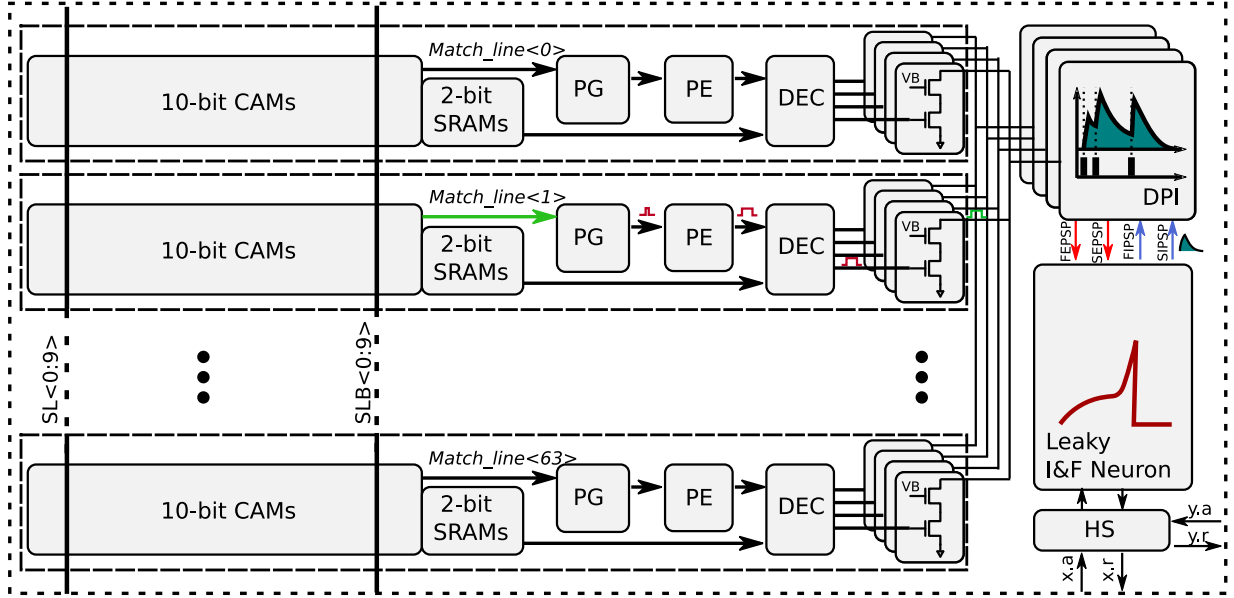


Fig. 9. Block diagram of one of the 256 computing nodes in each core. Each node comprises 64 mixed memory words, consisting of 10-bit CAM and 2-bit SRAM cells, 64 pulse generators circuits (PG), 64 pulse extenders circuits (PE), 64 pulse decoders (DECs),  $64 \times 4$  digital pulse to analog current converters, 4 DPI filters, one adaptive I&F neuron circuit, and one handshaking block (HS).

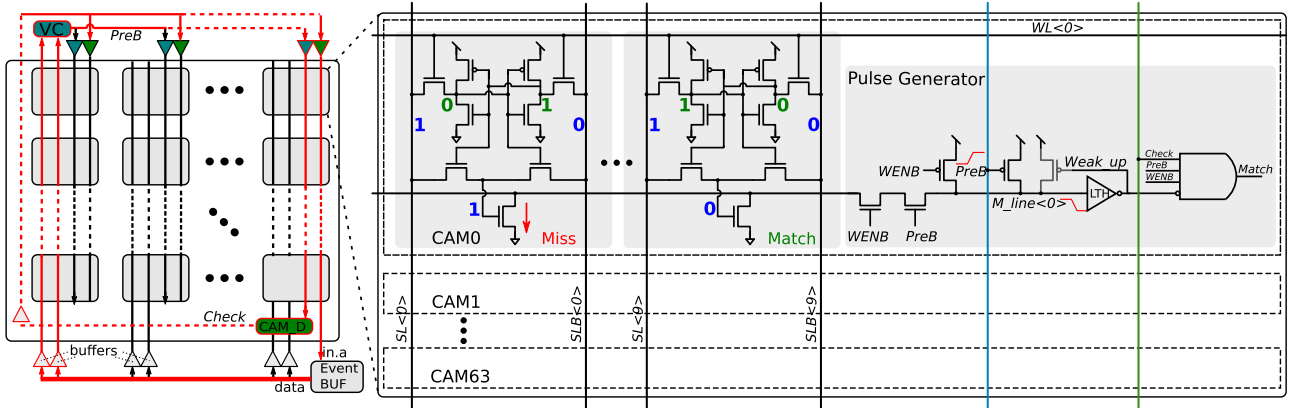


Fig. 10. Asynchronous content-addressable memory (CAM) circuit diagram. Left: a simplified  $16 \times 16$  CAM blocks in one core each having 64 words corresponding to 64 active synapses of a neuron. Right: Circuit details of one CAM word combined with one pulse generator circuit.

## V. EXPERIMENTAL RESULTS

The  $0.18 \mu\text{m}$  CMOS process used to fabricate the chip expects a core power-supply voltage of 1.8 V, however thanks to a careful design of the analog and asynchronous digital blocks, we could reduce the core supply voltage down to 1.3 V without any loss of functionality. The chip specifications, including speed and latency measurements, are outlined in Table II. As evident from this table, although the asynchronous routers deliver a high throughput within the chip, the overall system performance is limited by the speed of the I/O circuits. In larger designs this would not be a major problem, as the communication among neurons would mostly happen inside the chip. The other restricting factor is the broadcast time, i.e., the time that the CAM requires to process the incoming events. Also in this case, and similar to most memories designs that make use of

TABLE II  
BASIC SPECIFICATIONS OF THE MULTI-CORE NEUROMORPHIC PROCESSOR

Process Technology	$0.18 \mu\text{m}$ 1P6M
Supply voltage (core)	1.3 V–1.8 V
Supply voltage (I/O)	1.8 V–3.3 V
Die Size	$43.79 \text{ mm}^2$
Number of Neurons	1 k
Number of Synapses	64 k
Total Memory	64 k CAM + 4 k SRAM
I/O Speed	30 M events/s (input)/21 M events/s (output)
LUT Read Speed	750 Mb/s
Broadcast time <sup>1</sup>	27 ns
Latency across chips <sup>2</sup>	15.4 ns

<sup>1</sup>The broadcast time refers to the time it take to broadcast an incoming event to the core. It includes the broadcast buffer, the CAM search and the handshaking times.

<sup>2</sup>The latency for passing through the chip. It involves the R3 router and on-chip interconnects latency, taking in account the capacitance load of the output channel.

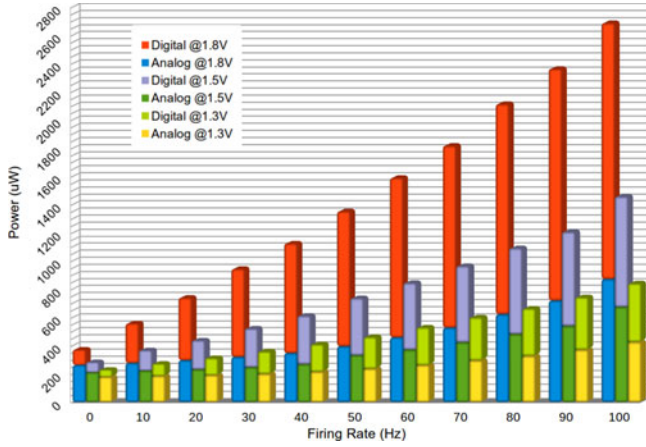


Fig. 11. Power dissipation measured for different supply voltage settings as a function of different average firing rates of all the neurons of the chip (worst case scenario). The firing rate is set by injecting a constant DC current to the neuron membrane capacitance. In this experiment, all neurons have active connections to 25% of all neurons in the chip, assuming the destination neurons for each spike resides across four cores. This measurement does not include the effect of synaptic currents (synaptic input currents neurons are replaced by the DC current injection for better control of their average firing rate)

TABLE III  
ENERGY CONSUMPTION OF THE MAIN OPERATIONS

Operation	1.8 V	1.3 V
Generate one spike	883 pJ	260 pJ
Encode one spike and append destinations	883 pJ	507 pJ
Broadcast event to same core	6.84 nJ	2.2 nJ
Route event to different core	360 pJ	78 pJ
Extend pulse generated from CAM match	324 pJ	26 pJ

asynchronous interfaces, we made worst-case scenario timing assumptions that guarantee correct functionality of the CAM circuits block (see Appendix for details). In the current design, we set the broadcast time to be 27 ns. Also this will not be a critical limitation in large scale multi-core designs, as the CAM cells of different cores operate in parallel.

Fig. 11 shows the average power dissipation measures, for different power-supply voltage settings, in a worst-case scenario condition in which all neurons of the chip are firing, at different average firing rates. The power usage of the major circuits in the neuromorphic processor is reported in Table III.

Despite the use of a 0.18  $\mu\text{m}$  CMOS process, and thanks to the mixed signal analog/digital and asynchronous design strategies adopted, the chip proposed achieves power consumption and latency figures that are comparable to analogous state-of-the-art architectures fabricated with more advanced scaled technology nodes. In Table IV we provide a detailed comparison between the specifications of this neuromorphic prototype chip and of recently proposed analogous neuromorphic systems.

The throughput of the local event-delivery circuitry and the routing networks are important factors for the overall scalability of the proposed architecture. At the on-chip core level, the throughput is determined by the broadcast time. In the current implementation the broadcast time is of  $\approx 27$  ns (leading to a bandwidth of  $\approx 38$  Mevents/sec) and the number of neurons

per core, i.e., 256. This results in a throughput that allows us to have 7200 fan-in per neuron in a network with the average firing rate of 20 Hz and 1400 fan-in at 100 Hz. As these are digital circuits, the throughput in the local core is expected to improve significantly when implemented in more advanced processes. At the large-scale network level, the “latency across chip” figure (which measures  $\approx 15.4$  ns in the current implementation) determines how many cores can be reliably integrated in a Printed Circuit Board (PCB) board. As this number is experimentally measured, it includes the latency of input pins, R3 router and output pins. In a many-core large chip design, the latency of the I/O pins would no longer impact the R3 throughput. In our 0.18  $\mu\text{m}$  prototype, R3 has the latency of 2.5 ns, delivering 400 Mevent/sec. According to circuit simulation studies [32], the throughput of the R3 router can reach up to 1 Gevents/sec in a 28 nm process. Thanks to the hierarchical structure of the routing architecture, a high percentage of local activity of a clustered network is sorted out by the R2 and R1 routers without need to involving the R3 routers. Therefore the traffic at the top level of hierarchy significantly decreases in comparison to that of a plain 2D mesh architecture. Furthermore, being implemented using only split/merge and decrements blocks, without any look-up table or feedback mechanism, the R3 router was carefully designed to have a simple and feed-forward structure. This structure provides more opportunity to increase the throughput by increasing the number of pipeline stages in future revision of this work.

#### V. Example Application: Convolutional Neural Networks

The architecture we proposed, and the prototype chip implementation used to validate it can be applied to a wide range of network types, ranging from biophysically realistic models of cortical networks, to more conventional machine learning and classical artificial neural networks. Here we use the prototype chip designed to implement CNNs. CNNs are a class of models originally inspired by the visual system, that are typically used to extract information from input images for classification. They are multi-layered networks whereby low-level features, such as edge orientations extracted by early layers, are subsequently combined to produce high-level feature detectors in later stages. To support experiments with multi-layer network structures, we developed a PCB board which hosts nine chips (of the type shown in Fig. 8). The inter-chip communication on the board is carried out by parallel input/output ports through direct wire/pin connections. The communication is directly managed by the programmable on-chip routers (R3). An additional on-board FPGA device is used for programming the on-chip memories, configuring the analog parameters and monitoring the neuron activities from all chips. The board is extendable as it has connectors on the four sides for interfacing to other instances of the same PCB. This feature extracting process makes the classification problem of the later stages much simpler. Therefore neural networks that combine several hidden layers of this form, known as deep neural networks (DNNs), can be efficiently trained to achieve very high performance on a wide range of visual and non-visual tasks [19]. Recently, pre-trained CNNs and

TABLE IV  
FEATURES OF THE MULTI-CORE NEUROMORPHIC PROCESSOR PRESENTED IN THIS WORK, AND OTHER RECENT ANALOGOUS DEVICES

	IBM Truenorth [4]	Spinnaker [5]	HiAER [13]	Neurogrid [3]	This work-CxQuad
Technology	28 nm	0.13 $\mu\text{m}$	0.13 $\mu\text{m}$	0.18 $\mu\text{m}$	0.18 $\mu\text{m}$
Neuron Type	Digital	Digital	Mixed	Mixed	Mixed
In core computation	Time multiplexing	Time multiplexing	Parallel	Parallel	Parallel
Fan-in/out	256/256	/1 k	x/1 k	x	64/4 k
Routing	on-chip	on-chip	on/off chip	on/off chip	on-chip
Energy per hop	2.3 pJ@0.77 V	1.11 nJ	x	14 nJ	17 pJ@1.3 V
Avg. Distance*	$2\sqrt{N}/3$	$\sqrt{N}/2$	x	x	$\sqrt{N}/3$

\*Average distance between any two nodes in the network of  $N$  neurons; HiAER and Neurogrid, hierarchical and tree-based network respectively, have utilized a combination of on-chip and off-chip resources for routing, therefore it is unclear what is the average distance between the nodes.

TABLE V  
AN EXAMPLE CNN FOR POKER CARD SUIT RECOGNITION EXPERIMENT

Parameter	Size
Input image	$32 \times 32$
Conv. kernels	$4 \times 8 \times 8$ , Stride = 2
Conv. layer output	$4 \times 16 \times 16$
Subsampling kernels	$2 \times 2$
Subsampling output	$4 \times 8 \times 8$
Fully-connected layer	$4 \times 64$

DNNs have been successfully mapped into spike-based hardware, achieving remarkable accuracy, while minimizing power consumption [33]–[36]. Furthermore, there are growing efforts towards the direct use of asynchronous event-based data produced by spiking sensors such as the DVS [37]–[42]. Here we tailored the design of the CNN for efficient real-time classification of event streams using an AER data-set recently made available [38] (see Table V). This data-set consists of a list of time-stamped events generated by an AER dynamic vision sensor while observing a very fast sequence of Poker cards flipped from a deck. All 52 cards of the deck are flipped in front of the vision sensor in about half a second producing a total of 0.5 million events with a peak rate of slightly above 8 Meps [43]. The events obtained in this way have been further processed to center the Poker card symbol in the center of  $31 \times 31$  image patches. Their weights have been set to detect vertical and horizontal edges as well as upward and downward vertices. The resulting  $16 \times 16 \times 4$  maps are then pooled into a layer comprising  $4 \times 8 \times 8$  maps. The activity of the silicon neurons in the pooling layer is then used as input to four populations of 64 neurons in the output layer. The all-to-all connections between pooling layer and output layer are tuned using an off-line Hebbian-like learning rule such that, for each input symbol, the 64 most active pooling layer neurons are strongly connected with the corresponding output neurons subgroup. We used 4 populations of 64 neurons, rather than just 4 neurons in the output layer, to stabilize the performance, by using a majority rule. The class corresponding to the right Poker card suit is thus determined by the most active population, during the presentation of the input pattern (see Fig. 12). As evident from Fig. 12, the asynchronous event-based processing nature of this architecture allowed the system to produce output results with extreme low-latency: the

classification result is available within less than 30 ms from the onset of the input stimulus. This figure was obtained without optimizing the network parameters for speed. The time constants in the analog circuits can be tuned to be much faster than the biologically plausible ones used in this demonstration (i.e., in the order of tens of milliseconds). The simplicity of the chosen problem was such that even a simple architecture such as the one described here, that used merely 2560 neurons was sufficient to achieve a 100% performance on the test data-set. The 9-chip board used for this experiment can support much larger and sophisticated networks (of up to 9 k neurons). It has been recently shown [33], [35] that if these networks are designed appropriately, they can tolerate the limited precision that affects the analog circuits in the chip, while preserving high accuracy figures that are comparable to those obtained by state-of-the-art Deep Neural Networks (DNNs) running on hardware consuming orders of magnitude more power.

One important and novel aspect of the hardware and framework proposed in this work is the flexibility offered by the memory optimized programmable routing scheme, that allows an efficient allocation of memory, synapse, and neural resources for a wide range of architectures, including CNNs. This is evident if one analyzes the amount of resources required by comparable architectures, such as the one proposed in [4], for different types of CNNs architectures, as recently reported in [36]. We analyzed the memory size for CNN models implemented on TrueNorth. The type of neuron and synapse models implemented in the two hardware platforms are very similar, therefore we'd expect similar classification performance if those networks were to be implemented on the proposed platform. Here we consider the scaling that we would obtain if we were to implement those CNN networks on our hardware platform. For TrueNorth, we observed a roughly quadratic relation between the number of hardware cores used and the number of neurons required by the network, despite the filter size being fixed by design in agreement with the hardware constraints (Fig. 13). This poor scaling derives from the fact that in TrueNorth it is necessary to allocate additional whole cores dedicated exclusively to routing events, to increase fan-out figures as required by the models. As our design comprises enough fan-in and fan-out memory resources per core, no additional resources need to be allocated, and scaling is linear with CNN size. This is a particularly relevant benefit if one considers that CNN networks being deployed in real-world

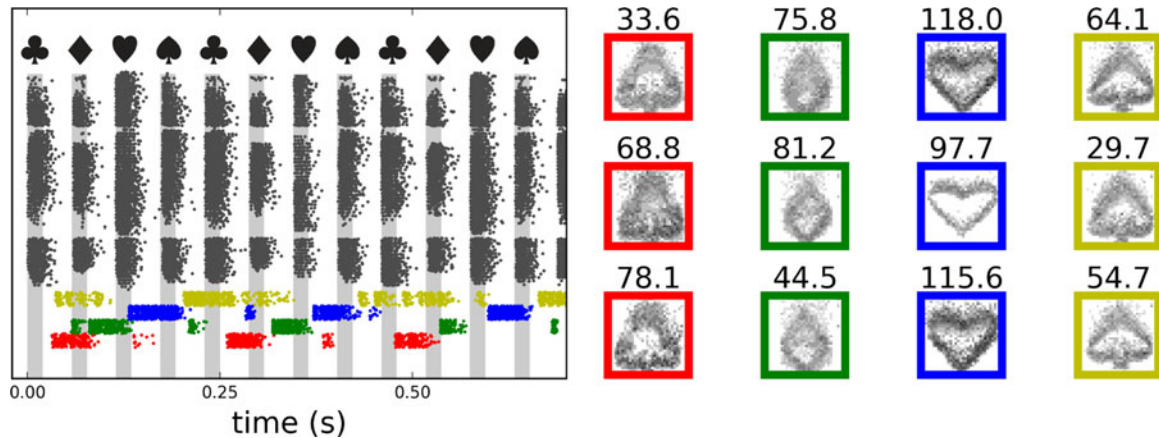


Fig. 12. CNN results of Poker card suit recognition experiment. Left panel: raster plot of input (grey) and output (colored) units. The symbols corresponding to the presented patterns are shown on the top. Right panel: image frames computed by aggregating the spiking outputs over time. In each panel, spikes aggregated from the input are shown with spike frequency encoded in grey levels, from 0 (white) to 400 Hz (black). The spiking data for each panel corresponds to the vertical grey bars in the raster plot on the left. The color of the panel borders encodes the estimated Poker card suit. It is determined by identifying the most active population of neurons in the output layer (with corresponding firing rate in Hz on top of each panel). The firing rates reported have been determined by the spike count in a 20 ms window delayed by 24 ms from the time window of the input to consider the delaying effects of synaptic integration. The input streams for each symbol have been manually separated for visual clarity.

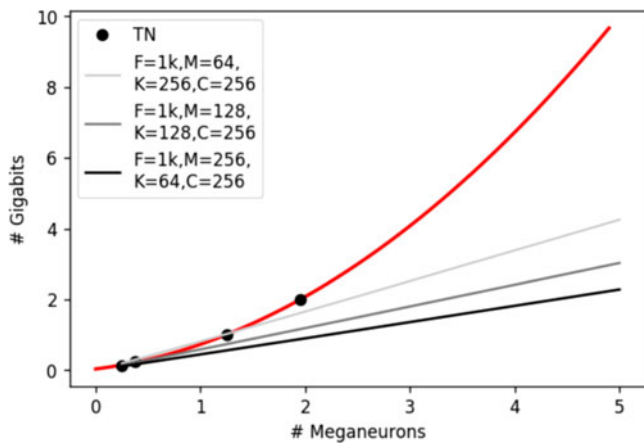


Fig. 13. Memory scaling comparison between the TrueNorth architecture [4] and this work. The number of bits used by the two architectures is plotted as a function of the CNN model size. For TrueNorth, 4 data points (black dots) are extrapolated from CNN benchmark models described in [36] and fitted with a quadratic function (red curve). The number of cores, and therefore the number of bits, used to implement the 4 models scales approximately quadratically with the size of the models (red line). This is likely due to the fact that in this architecture extra neuro-synaptic cores need to be used to expand neuron fan-in and fan-out for routing. In the proposed architecture instead, no additional cores are required for routing. Hence the scaling is linear with model size (dark lines, different shades represent different parameter choices). The prototype chip fabricated uses  $KM/C = 64$ . The scaling plots were computed from (2), but adding 2 extra bits per neuron for 4 synaptic weight types as in [36].

applications can have hundreds of layers and tens of thousands of neurons.

## VI. DISCUSSION

One of the most appealing features of neuromorphic processors is their ability to implement massively parallel computing architectures with memory and computation co-localized within their computational nodes. In addition to enabling ultra low-power data-driven processing, this feature allows for the

construction of scalable systems for implementing very large scale neural networks, without running into the von Neumann bottleneck problem [14], [15], and in other data communication bottleneck problems typical of centralized systems. However, distributed memory/computing systems come at the price of non-trivial routing overhead. Neuromorphic solutions that have optimized this overhead and, with it, the communication bandwidth, have sacrificed flexibility and programmability [3]. On the other hand, solutions that have maximized network configurability, have sacrificed silicon real-estate for on-chip memory [4], or resorted to using external memory banks [5] (and therefore eliminated the advantage of having memory and computation co-localized). In this work we presented a scalability study for neuromorphic systems that allows network configuration programmability and optimization of area and power consumption at the same time. This is especially important for the configuration of different classes of sensory-processing neural networks that are not restricted to classical CNNs and DNNs architectures, and that can be used to process real-time streaming data *on the fly*, without having to resort to saving input data in external memory structures (be it DRAM or other forms of solid-state storage).

While there have been ad-hoc solutions proposed in the literature for utilizing off-chip memory more efficiently in neuromorphic systems [44], there is no consensus around a systematic approach that would explicitly allow to trade-off flexibility and memory to meet the requirements of specific applications. The theoretical framework we proposed allows to choose an optimal trade-off point between network configuration flexibility and routing memory demands. The trade-offs and design points we chose for the prototype device built to validate our approach were determined by the study of cortical networks in mammalian brains [45]–[47]. In particular, our solution profits from the use of strategies observed in anatomically realistic topologies found in biology, namely to express dense clusters of connectivity



that are interconnected by few long range connections. These choices resulted in a novel architecture that incorporates distributed and heterogeneous memory structures, with a flexible routing scheme that can minimize the amount of memory required for a given network topology, and that supports the most common feed-forward and recurrent neural networks. The use of on-chip heterogeneous memory structures (such as CAMs and SRAMs cells) makes this architecture ideal for exploiting the emerging memory structures based on nano-scale resistive memories [16], [48], [49].

## VII. CONCLUSIONS

In this work we presented a two-stage routing scheme which minimizes the memory requirements needed to implement scalable and reconfigurable spiking neural networks with bounded connectivity. We used this scheme to solve analytically the trade-off between “point-to-point” connectivity, which increases memory budget in favor of connection specificity, and “broadcasting”, which reduces memory budget by distributing the same signal across populations of neurons. We presented QDI circuits and building blocks for implementing this routing scheme in asynchronous VLSI technology, and presented a prototype neuromorphic processor that integrates such building blocks together with mixed signal analog/digital neuron and synapse circuits. We showed that even with the conservative 0.18  $\mu\text{m}$  VLSI technology used, the power consumption of the prototype neuromorphic processor chip fabricated is comparable to state-of-art digital solutions. To demonstrate the features of such architecture and validate the circuits presented, we tiled multiple neuromorphic processors together and configured the setup to implement a three layer CNN. We applied the network to an event-based data-set and showed how the system can produce reliable accurate results, using extremely low power and latency figures. As scaling studies have demonstrated that such architecture can outperform the current state-of-the-art systems when implemented using a 28 nm Fully-Depleted Silicon on Insulator (FDSOI) process [32], we are confident that such approach can lead to the design of a new generation of neuromorphic processors for solving a wide range of practical applications that require real-time processing of event-based sensory signals, using ultra low-power, low latency, and compact systems.

## APPENDIX

### A. Routing Memory Minimization Constraints

Here we provide an intuitive explanation of why the two-stage routing scheme presented in Section II minimizes memory usage. First, consider a simple case in which two subgroups of  $K$  neurons project only within their groups. In this case the two groups correspond in fact to two separate networks and there is no need to store more than  $K$  words (which we shall call tags herein) to identify the neurons and thus to implement the connectivity for this network. Obviously having a larger network with more groups that share the same property of local connectivity doesn't affect  $K$ , hence  $K$  is constant with the number of neurons in the network. It is clear that adding one

connection from one group to an other may potentially cause an address collision, i.e., two neurons with the same tag project onto the same population, and therefore more than  $K$  tags are required in this case in order to implement different connectivity patterns for those neurons. If few connections exist between different clusters, i.e., in the case of sparse long-range connectivity, the total number of tags still scales slowly with the number of neurons because the number of address collisions is low, furthermore it can be kept under control by tag re-assignment. Although the particular number of  $K$  tags for a network depends on the actual specific connectivity, its average value at least for a given class of networks scales nicely with network size for the above reasons. An analogous situation appears if the neurons in one group never project back to the same group, as for example in a feed-forward network. These are deliberately oversimplified cases but in many scenarios neural networks do show clustering and grouping properties. It is clear that in such situations a  $K$ -tag based scheme for implementing the connectivity can be harnessed to gain in memory efficiency over a traditional scheme that requires to store  $N$  different identities and their connectivity. Next, we show a more systematic derivation of the theoretical constraints for optimizing digital memory in neuromorphic hardware implementations of clustered neural networks.

The optimal design point must satisfy the following requirements:

- 1)  $F \geq M^*$
- 2)  $C \geq M^*$

If the first requirement is not met and  $M^* > F$ :

$$\sqrt{\frac{F \log_2(\alpha N)}{\alpha \log_2(\alpha C)}} > F$$

$$\stackrel{\alpha=1}{\Rightarrow} N^{1/F} > C$$

Therefore,  $M^*$  is a valid design point if the cluster size meet this condition:  $C \geq N^{1/F}$ . This is a very safe constraint: for example even when the total neuron count is in the  $10^{10}$  range, a fan-out as small as 10 would require a cluster size of  $C \geq 10$  to be able to have an optimal choice of  $M^*$ . Since typical fan-out values are actually in the  $10^3$ – $10^4$  range, this requirement imposes very few constraints on the cluster size. The total number of neurons  $N$  would have to be larger than  $10^{10^3}$  before the right hand side of the constraint would be 10 or larger.

The second requirement indicates that the cluster size must be greater than a minimum size ( $C \geq M^*$ ) to support the anticipated fan-out.

$$C \geq \sqrt{\frac{F \log_2(\alpha N)}{\alpha \log_2(\alpha C)}}$$

which leads to:

$$\sqrt{F \log_2 \alpha N} \leq \sqrt{\alpha C} \sqrt{\log_2 \alpha C}$$

$$C \sqrt{\log_2(C)} \geq \sqrt{F \log_2(N)} \quad \text{for } \alpha = 1$$

This constraint is much more restrictive than the first one. For example, if we take typical values of  $F = 5000$ , and  $N = 10^{10}$ , then clusters need to be  $C \geq 152$ .

Conversely, if we pick a cluster size  $C = 256$  with  $\alpha = 1$  (i.e., with 256 tags), then the optimal value of  $M$  would be  $M^* = 144$ . In this case, the network requires a first-level fan-out of 35, followed by a second cluster-level fan-out of 144 for a fan-out of 5040 and the storage per neuron would be  $424.26 \sqrt{\log_2 N}$  bits.

### B. Communicating Hardware Process (CHP)

Here is a list of the most common CHP commands that cover the design of all the blocks presented in this paper:

- 1) Send:  $X ! e$  means send the value of  $e$  over channel  $X$ .
- 2) Receive:  $Y ? v$  means receive a value over channel  $Y$  and store it in variable  $v$ .
- 3) Probe: The boolean expression  $X$  is true if a communication over channel  $X$  can complete without suspending.
- 4) Sequential Composition:  $S; T$
- 5) Parallel Composition:  $S \mid T$  or  $S, T$
- 6) Assignment:  $a := b$ . This statement means “assign the value of  $b$  to  $a$ .” We also write  $a \uparrow$  for  $a := \text{true}$ , and  $a \downarrow$  for  $a := \text{false}$ .
- 7) Selection:  $[G1 \rightarrow S1 \mid \dots \mid Gn \rightarrow Sn]$ , where  $Gi$ ’s are boolean expressions (guards) and  $Si$ ’s are program parts. The execution of this command corresponds to waiting until one of the guards is true, and then executing one of the statements with a true guard. The notation  $[G]$  is shorthand for  $[G \rightarrow \text{skip}]$ , and denotes waiting for the predicate  $G$  to become true. If the guards are not mutually exclusive, we use the vertical bar “ $\mid$ ” instead of “ $\mid\mid$ .”
- 8) Repetition:  $*[G1 \rightarrow S1 \mid \dots \mid Gn \rightarrow Sn]$ . The execution of this command corresponds to choosing one of the true guards and executing the corresponding statement, repeating this until all guards evaluate to false. The notation  $*[S]$  is short-hand for  $*[\text{true} \rightarrow S]$ .

### C. CHP, HSE, and PR Examples or Asynchronous Circuits Used in the Routing Scheme

See Listing 4,5,6.

### D. Asynchronous Content-Addressable Memory (CAM) Timing Assumptions

In order to guarantee the correct handshaking communication between the local router (R1) and the CAM array, it is necessary to make appropriate timing assumptions. Here we describe the assumptions that were made in the design of the asynchronous CAM array. Initially, without the presence of input data, the output of Event Buffer (EB) is in neutral state and all the search lines are low:  $SL \langle 9 : 0 \rangle = 0$  and  $SLB \langle 9 : 0 \rangle = 0$ . Therefore the Validity Check (VC) block, placed at the top-right-hand side of the array in the layout (see also Fig. 10), sets  $PreB$  to 0 and consequently, all the MLs are pre-charged to high. Upon receiving the events, the buffers start broadcasting and driving the data lines in entire array. The  $VC$ , the last element in the

```

chp{
  *[[in1 → in1?s; out!s
    | in2 → in2?s; out!s
  ]]
}

hse{
  *[[ in1arb_out → x+;
    out.b[i].d[j] := in1.b[i].d[j];
    in1.a+; en1-;
    ([out.a]; x-; out.b[i].d[j]-;
    [~out.a]), (~in1arb_out);
    in1.a-; en1+
  ]]
  in2arb_out → x+;
  out.b[i].d[j] := in2.b[i].d[j];
  in2.a+; en2-;
  ([out.a]; x-; out.b[i].d[j]-;
  [~out.a]), (~in2arb_out);
  in2.a-; en2+
  ]]

  ||

  *[[in1.v & en1 → in1arb_in+;
    [~in1.v & ~en1]; in1arb-]

  ||

  *[[in2.v & en2 → in2arb_in+;
    [~in2.v & ~en2]; in2arb-]

  ||

  *[[in1arb_in → in1arb_out+;
    [~in1arb_in]; in1arb_out-
    | in2arb_in → in2arb_out+;
    [~in2arb_in]; in2arb_out-
  ]]
}

```

Listing 4: Merge.

```

chp{
  *[[v(in )]; [ctrl0 → out0↑
    | ctrl1 → out1↑];
    [n(in ) ^ n(ctrl)];
    out0↓, out1↓]
}

```

Listing 5: Controlled-Split.

```

chp{
  *[[ IN?x ; OUT!x ]
}

```

Listing 6: Buffer.

array to receive the valid data, eventually asserts  $PreB$  to high. This signal is in turn used to enable the comparison between the input (presented on data lines) and the CAM words content by sending the enable signal across the whole array from top-left to bottom-right. The duplicate CAM cell  $CAM\_D$ , placed at the opposite corner to the  $VC$  block (at the bottom-right-hand side of the CAM array), is assumed to be the last one to get the enable signal  $PreB$ . This duplicate cell is designed to produce a *miss* signal with the worst case (that is when only one bit is a miss in its 10-bit CAM word) for any data presented on search lines. Once its ML  $M\_line\_D$  is discharged, which guarantees that the

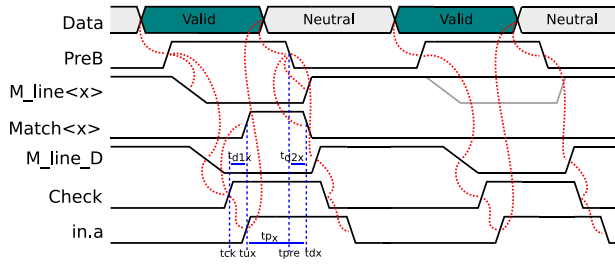


Fig. 14. CAM's 4-phase hand-shaking protocol.

comparison between input data lines and all CAMs words have been finished. At this point *Check* signal is being driven to high and is sent across the array. This signal then lets the CAM words with active MLs produce a *match(hit)* signal. The *Check* signal eventually reaches the *EB* block as the acknowledgment from the array. The *EB* circuits then de-asserts data and sets data lines to their neutral state, which lowers the *PreB*. Again, the *PreB* signal is sent from top-left to bottom-right to reset all the *Match* lines to low as well as to reset all MLs. As soon as the ML of the dummy CAM\_D, word is lowered, the *Check* signal is de-asserted and the handshaking is completed at this point. Although the local communication is not optimized for speed, it is sufficient to cover all the neurons in one core. The way we implemented the timing assumption guarantees small mismatch of pulse width of *Match* signals generated by different CAM words in the array. The pulse width is a critical parameter for the analog neural computations. It ensures that the mismatch between width of *Match* pulses generated in different synapses across the core is as small as possible. Assuming *PreB* and *Check* signals drive similar size load capacitances, The same buffer is used for sending these signals from top left to bottom right-hand side of the array. For a particular CAM word, CAM<sub>x</sub>,  $t_{d1x}$ , the delay between transmitting the “Check” signal and Match<x>, and  $t_{d2x}$ , the delay between *PreB* and Match<x> are about the same (see Fig. 14). The pulse width of a particular CAM<sub>x</sub> is  $t_{dx}t_{ux} = (t_{pre} + t_{d2x}) - (t_{ck} + t_{d1x})$ . And for  $t_{d1x}$  and  $t_{d2x}$ , the pulse width can be approximated to  $t_{pre} - t_{ck}$  which is not related to the physical position of the CAM.

In designing the asynchronous CAM array we made worst-case scenario timing assumptions to ensure the correct operation of the circuits. Let's consider the case in which the dual-rail data from the output of Event Buffer (EB) of Fig. 10 is neutral with all search lines:  $SL\langle 9:0 \rangle = 0$  and  $SLB\langle 9:0 \rangle = 0$ . The Validity Check (VC) block at the top-right-hand side of the array in Fig. 10 checks the data state and assigns *PreB* to 0 for the neutral state. All MLs are consequently pre-charged to high.

Once EB gets events from the previous stage, i.e., from the core router R1, it pushes the new data to dual-rail data lines and broadcasts it to the whole array through broadcasting buffers. After the searching lines have successfully set-up the new data, VC is assumed to be the last one in this array to get the valid data. This is in turn used to enable the CAMs comparisons by transmitting the enable signal to the whole core from top-left to bottom-right. The duplicate CAM cell CAM\_D, placed at the bottom-right-hand side of the CAM array, is assumed to be the last one to get the enable signal *PreB* for comparing.

This duplicate cell is designed to always get a miss with the worst case (only one bit is a miss in its 10-bit CAM word for discharging the ML) for any data presented on search lines. Once its ML *M\_line\_D* is discharged, which guarantees that all CAMs in this array have finished comparing, an inverted signal *Check* is asserted to high and sent to left-top of the array. Then it is buffered to the whole array from left-top to right-bottom. All MLs in this array will apply an AND operation with *Check*, *PreB* and ML, and CAM words with match state will get a high Match. The *Check* signal will finally arrive at EB as the acknowledge signal of its valid output data. The EB will then de-assert the data and set the data lines to neutral again, which will cause the *PreB* from VC to be set to 0. Again, the high to low transition of *PreB* is transmitted from top-left to bottom-right of the layout, to reset all high Match to low as well as to reset all MLs. As soon as this happens the ML of the dummy cell CAM\_D (which has been positioned physically as the last in the array), is reset again and the signal *Check* is set to low, to finish the handshaking. Assuming that *PreB* and *Check* have similar load capacitances in the whole array and that the same buffer is used for transmitting from top left to bottom right-hand side of the array, then for a particular CAM word CAM<sub>x</sub> in a match state, the delay  $t_{d1x}$  between transmits of *Check* and Match<x> and the delay  $t_{d2x}$  between *PreB* and Match<x> will be similar.

Another critical circuit is the one responsible for extending input pulses. Since that pulse width is also one critical parameter of analog computing, the pulse width circuit has to minimize the effect of mismatch, such that pulses generated in different synapses across the core should be as similar as possible. Fig. 14 shows the sequence of operations from the events received at the input of each to the signals routed to the synapses in the core. At the very beginning, dual-rail data from output of Event Buffer (EB) is “neutral” with all search lines,  $SL\langle 9:0 \rangle = 0$  and  $SLB\langle 9:0 \rangle = 0$ . The Validity Check (VC) block at the right-top of the array will check the data state and assign *PreB* to “0” for the “neutral” state. All MLs are consequently pre-charged to “high”. Once EB gets events from the previous stage, i.e. the local router R1, it will push the new data to dual-rail data lines and broadcast it to the whole array through broadcasting buffers. After searching lines have successfully set-up new data, VC is assumed to be the last one in this array to get the valid data, check dual-rail data presented on search lines and assert *PreB* to “1” for the “valid” state. This is in turn used to enable the CAMs comparisons by transmitting the “enable” signal the whole core from left-top to right-bottom. The duplicate CAM cell CAM\_D placed at the right-bottom of the CAM array is assumed to be the last one to get the enable signal *PreB* for comparing. This duplicate cell is designed to always get “miss” with the worse case (only one bit is miss in its 10-bit CAM word for discharging the ML) for any data presenting on search lines. Once its ML *M\_line\_D* is discharged which can guarantee that all CAMs in this array have finished comparing, a inverted signal *Check* is asserted to “high” and sent to left-top of the array and then buffered to the whole array from left-top to right-bottom. All MLs in this array will do AND operation with *Check*, *PreB* and ML, CAM words with “match” state



will get “high” *Match*. The *Check* signal will finally arrive at EB as the acknowledge signal of its valid output data. The EB will then dessert data and set data lines to “neutral” again, which will cause the *PreB* from VC to be “0”. Again, the “jumping from high to low” of *PreB* is still transmitted from left-top to right-bottom to reset all “high” *Match* to “low” as well as reset all MLs. As soon as the ML of duplicate cell CAM\_D which is assumed to be the last one in the array has been reset again, *Check* will go low and set in.a to low to finish the handshaking.

The local communication is not optimized for speed, however it minimizes the mismatch of the pulse width generated by different CAM words with *match* states distributed in the whole array. Due to the small number of neurons in each core, the speed of operations is already sufficient with this scheme. Assuming *PreB* and *Check* have similar load capacitances in the whole array and that the same buffer is used for transmitting from top-left to right-bottom of the array, then for a particular CAM word  $CAM_x$  in a *match* state, the delay  $t_{d1x}$  between transmits of *Check* and *Match*  $<x>$  and the delay  $t_{d2x}$  between *PreB* and *Match*  $<x>$  will be similar (see Fig 14). The pulse weight of a particular  $CAM_x$  is  $t_{dx} - t_{ux} = (t_{pre} + t_{d2x}) - (t_{ck} + t_{d1x})$ . For similar  $t_{d1x}$  and  $t_{d2x}$ , the pulse weight can be approximated to  $t_{pre} - t_{ck}$  which is no more related to the physical position of the CAM.

#### ACKNOWLEDGMENT

The authors would like to thank Prof. R. Manohar, Computer Systems Lab, Yale University, for providing the tutorials and tips on the design of asynchronous circuits, as well as CAD tools for the synthesis and verification of the asynchronous circuits. We thank our colleagues at the Institute of Neuroinformatics in Zurich for stimulating discussions.

#### REFERENCES

- [1] S. Moradi and G. Indiveri, “An event-based neural network architecture with an asynchronous programmable synaptic memory,” *IEEE Trans. Biomed. Circuits Syst.*, vol. 8, no. 1, pp. 98–107, Feb. 2014.
- [2] N. Qiao *et al.*, “A re-configurable on-line learning spiking neuromorphic processor comprising 256 neurons and 128k synapses,” *Frontiers Neurosci.*, vol. 9, pp. 1–17, 2015.
- [3] B. V. Benjamin *et al.*, “Neurogrid: A mixed-analog-digital multichip system for large-scale neural simulations,” *Proc. IEEE*, vol. 102, no. 5, pp. 699–716, May 2014.
- [4] P. A. Merolla *et al.*, “A million spiking-neuron integrated circuit with a scalable communication network and interface,” *Science*, vol. 345, no. 6197, pp. 668–673, Aug. 2014.
- [5] S. Furber, F. Galluppi, S. Temple, and L. Plana, “The SpiNNaker project,” *Proc. IEEE*, vol. 102, no. 5, pp. 652–665, May 2014.
- [6] S. Scholze *et al.*, “A 32Gbit/s communication SoC for a waferscale neuromorphic system,” *Integr. Very Large Scale Integr. J.*, vol. 45, no. 1, pp. 61–75, 2012.
- [7] S. Brink, S. Nease, and P. Hasler, “Computing with networks of spiking neurons on a biophysically motivated floating-gate based neuromorphic integrated circuit,” *Neural Netw., Official J. Int. Neural Netw. Soc.*, vol. 45, pp. 39–49, 2013.
- [8] S. Moradi and G. Indiveri, “A VLSI network of spiking neurons with an asynchronous static random access memory,” in *Proc. IEEE Biomed. Circuits Syst. Conf.*, Nov. 2011, pp. 277–280.
- [9] S. Deiss *et al.*, “Address-event asynchronous local broadcast protocol,” 1994. [Online]. Available: <http://www.ini.uzh.ch/~amw/scx/aeprotocol.html>
- [10] K. Boahen, “Point-to-point connectivity between neuromorphic chips using address-events,” *IEEE Trans. Circuits Syst. II*, vol. 47, no. 5, pp. 416–34, May 2000.
- [11] P. Dayan and L. Abbott, *Theoretical Neuroscience: Computational and Mathematical Modeling of Neural Systems*. Cambridge, MA, USA: MIT Press, 2001.
- [12] C. Zamarreño-Ramos, A. Linares-Barranco, T. Serrano-Gotarredona, and B. Linares-Barranco, “Multicasting mesh AER: A scalable assembly approach for reconfigurable neuromorphic structured AER systems. Application to convNets,” *IEEE Trans. Biomed. Circuits Syst.*, vol. 7, no. 1, pp. 82–102, Feb. 2013.
- [13] J. Park, T. Yu, S. Joshi, C. Maier, and G. Cauwenberghs, “Hierarchical address event routing for reconfigurable large-scale neuromorphic systems,” *IEEE Trans. Neural Netw. Learn. Syst.*, vol. 28, no. 10, pp. 2408–2422, Oct. 2017.
- [14] J. Backus, “Can programming be liberated from the Von Neumann style?: A functional style and its algebra of programs,” *Commun. ACM*, vol. 21, no. 8, pp. 613–641, 1978.
- [15] G. Indiveri and S.-C. Liu, “Memory and information processing in neuromorphic systems,” *Proc. IEEE*, vol. 103, no. 8, pp. 1379–1397, Aug. 2015.
- [16] H. Akinaga and H. Shima, “Resistive random access memory (ReRAM) based on metal oxides,” *Proc. IEEE*, vol. 98, no. 12, pp. 2237–2251, Dec. 2010.
- [17] E. Chicca, F. Stefanini, C. Bartolozzi, and G. Indiveri, “Neuromorphic electronic circuits for building autonomous cognitive systems,” *Proc. IEEE*, vol. 102, no. 9, pp. 1367–1388, Sep. 2014.
- [18] A. Litwin-Kumar and B. Doiron, “Formation and maintenance of neuronal assemblies through synaptic plasticity,” *Nature Commun.*, vol. 5, 2014, Art. no. 5319.
- [19] Y. LeCun, Y. Bengio, and G. Hinton, “Deep learning,” *Nature*, vol. 521, no. 7553, pp. 436–444, 2015.
- [20] R. Douglas and K. Martin, “Neural circuits of the neocortex,” *Annu. Rev. Neurosci.*, vol. 27, pp. 419–51, 2004.
- [21] D. Muir *et al.*, “Embedding of cortical representations by the superficial patch system,” *Cerebral Cortex*, vol. 21, no. 10, pp. 2244–2260, 2011.
- [22] S. Moradi, N. Imam, R. Manohar, and G. Indiveri, “A memory-efficient routing method for large-scale spiking neural networks,” in *Proc. IEEE Eur. Conf. Circuit Theory Des.*, 2013, pp. 1–4.
- [23] A. J. Martin, “The limitations to delay-insensitivity in asynchronous circuits,” in *Proc. 6th MIT Conf. Adv. Res. VLSI*, 1990, pp. 263–278.
- [24] C. A. R. Hoare, *Communicating Sequential Processes*. Upper Saddle River, NJ, USA: Prentice-Hall, 1985.
- [25] A. Martin and M. Nystrom, “Asynchronous techniques for system-on-chip design,” *Proc. IEEE*, vol. 94, no. 6, pp. 1089–1120, Jun. 2006.
- [26] R. Manohar, “Reconfigurable asynchronous logic,” in *Proc. IEEE Custom Integr. Circuits Conf.*, 2006, pp. 13–20.
- [27] E. Izhikevich, *Dynamical Systems in Neuroscience: The Geometry of Excitability and Bursting*. Cambridge, MA, USA: MIT Press, 2006.
- [28] R. Naud, N. Marcille, C. Clopath, and W. Gerstner, “Firing patterns in the adaptive exponential integrate-and-fire model,” *Biol. Cybern.*, vol. 99, no. 4–5, pp. 335–347, Nov. 2008.
- [29] C. Bartolozzi and G. Indiveri, “Synaptic dynamics in analog VLSI,” *Neural Comput.*, vol. 19, no. 10, pp. 2581–2603, Oct. 2007.
- [30] T. Delbruck, R. Berner, P. Lichtsteiner, and C. Dualibe, “32-bit configurable bias current generator with sub-off-current capability,” in *Proc. IEEE Int. Symp. Circuits Syst.*, 2010, pp. 1647–1650.
- [31] K. Pagiamtzis and A. Sheikholeslami, “Content-addressable memory (CAM) circuits and architectures: A tutorial and survey,” *IEEE J. Solid-State Circuits*, vol. 41, no. 3, pp. 712–727, Mar. 2006.
- [32] N. Qiao and G. Indiveri, “Scaling mixed-signal neuromorphic processors to 28 nm FD-SOI technologies,” in *Proc. IEEE Biomed. Circuits Syst. Conf.*, 2016, pp. 552–555.
- [33] P. U. Diehl, D. Neil, J. Binas, M. Cook, S.-C. Liu, and M. Pfeiffer, “Fast-classifying, high-accuracy spiking deep networks through weight and threshold balancing,” in *Proc. Int. Joint Conf. Neural Netw.*, 2015.
- [34] Y. Cao, Y. Chen, and D. Khosla, “Spiking deep convolutional neural networks for energy-efficient object recognition,” *Int. J. Comput. Vis.*, vol. 113, no. 1, pp. 54–66, 2015.
- [35] D. Marti, M. Rigotti, M. Seok, and S. Fusi, “Energy-efficient neuromorphic classifiers,” *Neural Comput.*, vol. 28, pp. 2011–2044, 2016.
- [36] S. K. Esser *et al.*, “Convolutional networks for fast, energy-efficient neuromorphic computing,” *Proc. Nat. Acad. Sci.*, vol. 113, no. 41, pp. 11 441–1446, 2016.



- [37] J. A. Pérez-Carrasco *et al.*, "Mapping from frame-driven to frame-free event-driven vision systems by low-rate rate coding and coincidence processing—application to feedforward convnets," *IEEE Trans. Pattern Anal. Mach. Intell.*, vol. 35, no. 11, pp. 2706–2719, Nov. 2013.
- [38] T. Serrano-Gotarredona and B. Linares-Barranco, "Poker-DVS and MNIST-DVS. Their history, how they were made, and other details," *Frontiers Neurosci.*, vol. 9, p. 481, 2015.
- [39] J. A. Henderson, T. A. Gibson, and J. Wiles, "Spike event based learning in neural networks," arXiv: 1502.05777, 2015.
- [40] B. Zhao, R. Ding, S. Chen, B. Linares-Barranco, and H. Tang, "Feedforward categorization on AER motion events using cortex-like features in a spiking neural network," *IEEE Trans. Neural Netw. Learn. Syst.*, vol. 26, no. 9, pp. 1963–1978, Sep. 2015.
- [41] G. Orchard, C. Meyer, R. Etienne-Cummings, C. Posch, N. Thakor, and R. Benosman, "Hfist: A temporal approach to object recognition," *IEEE Trans. Pattern Anal. Mach. Intell.*, vol. 37, no. 10, pp. 2028–2040, Oct. 2015.
- [42] X. Lagorce, G. Orchard, F. Gallupi, B. E. Shi, and R. Benosman, "Hots: A hierarchy of event-based time-surfaces for pattern recognition," *IEEE Trans. Pattern Anal. Mach. Intell.*, vol. 39, no. 7, pp. 1346–1359, Jul. 2017.
- [43] L. Camunas-Mesa, C. Zamarreno-Ramos, A. Linares-Barranco, A. Acosta-Jimenez, T. Serrano-Gotarredona, and B. Linares-Barranco, "An event-driven multi-kernel convolution processor module for event-driven vision sensors," *J. Solid-State Circuits*, vol. 47, no. 2, pp. 504–517, Feb. 2012.
- [44] S. Davies, F. Gallupi, A. D. Rast, and S. B. Furber, "A forecast-based STDP rule suitable for neuromorphic implementation," *Neural Netw.*, vol. 32, pp. 3–14, 2012.
- [45] T. Binzegger, R. Douglas, and K. Martin, "A quantitative map of the circuit of cat primary visual cortex," *J. Neurosci.*, vol. 24, no. 39, pp. 8441–53, 2004.
- [46] R. Douglas and K. Martin, "Recurrent neuronal circuits in the neocortex," *Current Biol.*, vol. 17, no. 13, pp. R496–R500, 2007.
- [47] N. Markov and H. Kennedy, "The importance of being hierarchical," *Current Opin. Neurobiol.*, vol. 23, no. 2, pp. 187–194, 2013.
- [48] B. Rajendran *et al.*, "Specifications of nanoscale devices and circuits for neuromorphic computational systems," *IEEE Trans. Electron Devices*, vol. 60, no. 1, pp. 246–253, Jan. 2013.
- [49] G. Indiveri, E. Linn, and S. Ambrogio, "ReRAM-based neuromorphic computing," in *Resistive Switching: From Fundamentals of Nanoionic Redox Processes to Memristive Device Applications*. Weinheim, Germany: Wiley-VCH Verlag GmbH & Co. KGaA, 2016, pp. 715–735.



**Saber Moradi** received the Master's degree in electrical engineering from Sharif University of Technology, Tehran, Iran, in 2008 and the Ph.D. degree in electrical engineering from ETH Zurich, Zurich, Switzerland, focusing on bioinspired computing architectures and asynchronous circuits and systems. He is currently a Postdoctoral Researcher at Computer Systems Lab, Yale University, New Haven, CT, USA. In 2014, he joined Neuromorphic Lab at Samsung Electronics, where he was involved in the development of Samsung's Dynamic Vision Sensor chip and neuromorphic processors project. His work as Postdoctoral Researcher at Cornell Tech, NY, then Yale University, has been mainly focused on architectural design exploration for deep learning algorithms, neuromorphic multicore routing architectures and CMOS-NEMS neuromorphic circuits. His current research interests include artificial intelligence applications, high-performance deep learning hardware accelerator design, neuromorphic computing circuits and architectures, and event-driven computation and routing networks.



**Ning Qiao** (M'15) received the Bachelor's degree in microelectronics and solid-state electronics from Xi'an Jiaotong University, Xi'an, China, in 2006 and the Ph.D. degree in microelectronics from the Institute of Semiconductors, Chinese Academy of Sciences, China, in 2012, researching on ultra low-power low-noise mixed-signal circuits in SOI process. He is a Postdoctoral Researcher at the Institute of Neuroinformatics, University of Zurich and ETH Zurich, Switzerland. He joined the Institute of Neuroinformatics, University of Zurich and ETH Zurich as a Postdoctoral Researcher in 2012, focusing on developing mixed-signal multicore neuromorphic VLSI circuits and systems. His current research interests concern ultra-low-power subthreshold mixed-signal neuromorphic VLSI circuits and systems, parallel neuromorphic computing architectures and fully asynchronous event-driven computing and communication circuits and systems.



**Fabio Stefanini** received the Bachelor's (Laurea Breve) and the Master's degree (Laurea Magistrale) in physics from Sapienza University of Rome, Rome, Italy, in 2009 and 2013, respectively, with a focus on complex systems and collective behavior. He received the Ph.D. degree in physics from the Institute of Neuroinformatics, University of Zurich and ETHZ, Switzerland, researching on low-power hardware implementations and models of synaptic plasticity rules in spiking neural networks employed in category learning and classification and the Ph.D. degree in neuroscience from the Center for Neuroscience of Zurich, Switzerland. He is a Postdoctoral Research Scientist at Columbia University. He joined Columbia University as a Postdoctoral Research Fellow in 2014 focusing on the development of new theoretical models of memory systems with biologically plausible synaptic plasticity rules for continuous learning and on analyzing large datasets of brain imaging data from rodent hippocampus using decoding techniques. His current research interests concern the study of efficient neural codes for memory formation in biology and with theoretical models, biologically plausible neural network models for machine learning, hardware implementations of neural network models for ultrarapid categorization, continuous learning and efficient memory systems.



**Giacomo Indiveri** (SM'95) received the M.Sc. degree in electrical engineering and the Ph.D. degree in computer science from the University of Genoa, Genoa, Italy. In 2006, he attained the "habilitation" in Neuromorphic Engineering at the ETH Zurich Department of Information Technology and Electrical Engineering. He was a Postdoctoral Research Fellow in the Division of Biology, Caltech and at the Institute of Neuroinformatics, University of Zurich and ETH Zurich. He is a Professor at the Faculty of Science, University of Zurich, Switzerland. He received the ERC Starting Grant on "Neuromorphic processors" in 2011 and an ERC Consolidator Grant on neuromorphic cognitive agents in 2016. His research interests include the study of neural computation, with particular interest in spike-based learning and selective attention mechanisms, and in the hardware implementation of real-time sensory-motor systems using analog/digital neuromorphic circuits and emerging VLSI technologies.